Effect of Nitrogen and Phosphorus Doping of Reduced Graphene Oxide in the Hydrogen Evolution Catalytic Activity of Supported Ru Nanoparticles

Laura Mallón,[‡♣] Javier Navarro-Ruiz,[‡♦] Christian Cerezo-Navarrete,[‡♥] Nuria Romero,[♠] Iker del Rosal,[♦] Jordi García-Antón,[♣] Roger Bofill,[♣] Luis Miguel Martínez-Prieto,*[♥,♦] Karine Philippot,*[♠] Romuald Poteau*[♦] and Xavier Sala *[♣]*

AUTHORS ADDRESSES

♣ Departament de Química, Universitat Autònoma de Barcelona, 08193 Bellaterra (Catalonia), Spain.

♦ Université de Toulouse; INSA, UPS, CNRS; LPCNO (IRSAMC), 135 avenue de Rangueil, F-31077 Toulouse, France.

♥ ITQ, Instituto de Tecnología Química (CSIC-Universitat Politècnica de València), Av. de los Naranjos S/N 46022, Valencia, Spain.

♠ CNRS, LCC (Laboratoire de Chimie de Coordination), UPR8241, Université de Toulouse, UPS, INPT, Toulouse cedex 4 F-31077, France.

• IIQ, Instituto de Investigaciones Químicas (CSIC-Universidad de Sevilla), Avda. Américo Vespucio 49, 41092 Seville, Spain.

KEYWORDS: reduced graphene oxide, N-doping, P-doping, hydrogen evolution reaction, Ru nanoparticles, DFT simulations

ABSTRACT: Three different cathodic materials for the hydrogen evolution reaction (HER) consisting of Ru nanoparticles (NPs) supported onto a bare and two doped reduced graphene oxides (r-GO) have been studied. Ru NPs have been synthesized in-situ by means of the organometallic approach in the presence of each reduced graphene support (bare (rGO), N-doped (NH_2-rGO) and P-doped (P-rGO)). (HR)TEM, EDX, EA, ICP-OES, XPS, Raman and NMR techniques have been used to fully characterize the obtained rGO-supported Ru materials. These materials have been deposited onto a glassy carbon rotating disk electrode (GC-RDE) to assess their HER electrocatalytic activity at acidic pH. The results show that all three materials are stable under reductive conditions for at least 12 h, and that the heteroatom-doping of the graphene structure extremely increases the activity of the electrodes, especially for the case of Ru@P-rGO, where the overpotential at -10 $mA \cdot cm^{-2}$ decreases to only 2 mV. *Realistic* (based on experimental compositional data) modelling of the three rGO supports combined with DFT computational analysis of the electronic and electrocatalytic properties of the hybrid nanocatalysts allows to attribute the observed electrocatalytic performances to a combination of interrelated factors such as the distance of the Ru atoms to the dopped rGO support and the hydride content at the Ru NP surface.

INTRODUCTION

Climate change has become one of the main concerns of humanity. One way to tackle this issue is the use of renewable H_2 as a clean energy vector. This can be achieved using electrocatalysts able to reduce protons into hydrogen, with the help of green electricity, in the so-called hydrogen evolution reaction (HER).[1]

Graphene (G) possesses high surface area, stability and electronic conductivity, making it suitable for its use in electrocatalysis.[2] In addition, its electrocatalytic activity can be tuned by doping its structure with heteroatoms, such as N,[3,4,5,6] P,[4,5,6,7] S,[5,8] O,[5] B[5] and F,[5] where it has been observed by DFT calculations that N and O become negatively charged (electron acceptors for adjacent C), while B, S, P and F become positively charged (electron donors).[5]

Given the well-known electrocatalytic activity of heteroatom doped-G systems, many researchers have used these materials as supports to study the HER electrocatalytic activity of metallic nanoparticles (NPs). By taking advantage of the putative synergistic electronic transfer effects between the supports and the NPs, it is expected to obtain higher HER activities and lower η_{10} values. Furthermore, the use of G-based supports allows attaining more stable and better dispersed NPs by restraining their aggregation.[9,10]

Among the different metallic NPs of interest for HER, Ru has emerged in the last decade as an attractive option due to its almost optimal ruthenium-hydrogen bond strength and its elevated stability in the whole pH range.[11,12] The literature reports several examples with interesting low η_{10} values at acidic pH: 29 mV and 15 mV for 1.9 nm and 1.5 nm Ru NPs deposited on alginate-derived G and P-doped G, respectively, after a reductive activation process (Ru/G-r and Ru/P-G-r, respectively),[13] 55 mV for a 3.5 nm Ru NP-modified N-doped G aerogel (Ru-NGA),[14] 62 mV

for 2.1 nm Ru NPs embedded in N-doped carbon (Ru@NC),[15] 126 mV for 2-3 nm Ru NPs supported on N-doped carbon (Ru@CN)[16] and 53 mV for 3-7 nm Ru nanoclusters deposited at 750 °C on top of N-doped G (Ru/NG-750).[17]

Interestingly, some studies combining experimental electrochemical data and DFT calculations dealing with the effect of the interaction between Ru NPs and a doped-G structure to tune the overall HER electrocatalytic activity have been recently published.[18,19,20] Most of these studies intrinsically rely on the calculation of the hydrogen adsorption free energy, ΔG_{H^*}, a property considered as a descriptor for the HER in the framework of the seminal Nørskov electrochemical model.[21,22] From those, it has been demonstrated by ΔG_{H^*} calculations, Density of States (DOS) studies and charge distribution analysis that the presence of O atoms due to the oxidation of porous graphene reduces the ΔG_{H^*} value for the G-supported Ru NPs.[19] Furthermore, it has been shown by ΔG_{H^*} calculations, Bader charge computation and crystal orbital Hamilton population analysis that Ru NPs bind through a stable Ru–O–C bond to a reduced graphene oxide (rGO).[20] This Ru-O bond induces an electron deficiency on the Ru NPs, which in turn reduces the barriers for the HER, making ΔG_{H^*} closer to 0 kcal·mol^{-1} and the Ru–Ru bonds in the NP stronger. Also, it has been demonstrated by Kinetic Monte Carlo (KMC) simulations that for strong or moderate H-binding metals (such as Ru) containing a high amount of adsorbed H atoms, there is a spill-over of these H atoms from the NPs surface to the rGO surface that is beneficial for the HER process in alkaline media, diminishing the overpotentials.[23] Finally, other approaches combining different levels of theory have been recently used to study the mechanisms (kinetic properties) and mass transport phenomena induced by metallic systems deposited onto C-based or semiconductor supports.[24, 25, 26] Thus, for instance, ab initio molecular dynamics (AIMD) simulations have been employed to study the H_2 adsorption capacity and spill-over effect of Pd_4 and Pd_3P clusters anchored on

different G-surfaces.[24] However, to the best of our knowledge, these approaches have not yet been applied to Ru/rGO systems for HER electrocatalysis.

Additionally, Ru_2P NPs have also been deposited onto non-doped rGO[27] and N,P-co-doped C nanofibers,[28] achieving very competitive HER electrocatalytic activities at acidic pH (η_{10} as low as 22 mV and 15 mV, respectively). For the former, according to DFT calculations, partial electron transfer from the Ru_2P NPs to the surface sp^2-C atoms of rGO favors hydrogen adsorption and recombination,[27] and for the latter, the superior HER performance of the NPs is associated with the modification of their ΔG_{H^*} by the N,P-co-doped C surface, which boosts their proton adsorption and reduction capacities.[28] Thus, a positive effect in the HER electrocatalytic activity of Ru_2P NPs has been demonstrated with N,P-co-doped C-based supports. But, to the best of our knowledge, there is no literature report in which metallic Ru NPs have been deposited independently on top of N-doped and P-doped rGO supports and their differential HER electrocatalytic behavior studied both from the experimental and theoretical points of view in comparison with the non-doped rGO counterpart.

In this work, we study the effect of N- and P-doping of reduced graphene oxide in the HER electrocatalytic performance of rGO-deposited Ru NPs by using a full set of experimental ((HR)TEM, EDX, EA, ICP-OES, XPS, Raman, NMR and LSV) and theoretical (DFT analysis) tools. The NPs have been deposited on-top of the pre-formed rGO supports by slow decomposition of a Ru organometallic complex under hydrogen pressure,[29] allowing to obtain surface clean Ru NPs. Additionally, the use of rGO as a support decreases the concentration of oxygen-based groups at the surface, which may block the interaction between the organometallic precursor and the graphitic structure and prevent the formation of the NPs, as has recently been observed by some of us.[30] Furthermore, in contrast to the frequent practice of synthesizing the

rGO and the Ru NPs simultaneously by chemical reduction, the method used here allows fine-tuning the heteroatom-doping of the rGO prior to its use as a support. Finally, by using the experimental EA, XPS and Raman data of the supports we have built up realistic rGO theoretical surfaces onto which DFT calculations (d-band center and charge analysis, ΔG_{H^*} determination) have been performed with two different Ru-NP models. Volcano plots have been calculated in the framework of the Yang, Saidi and collaborators electrochemical model,[31,32] which is an improvement of the Nørskov model.[21,22] Both provide valuable theoretical framework for understanding the kinetics and mechanisms of HER. The variables that affect the electrochemical HER activity of the rGO-supported Ru NPs, such as the distance of the Ru atoms to the support or the hydride content of the Ru NP surface, have also been analyzed.

RESULTS AND DISCUSSION

The **Ru@rGO** and **Ru@NH$_2$-rGO** cathodic materials were previously synthesized by some of us for their use in catalytic processes other than HER.[30,33] We have enlarged this group of catalysts to the **Ru@P-rGO** counterpart to perform a full experimental and theoretical comparative study of the effect of independent N- and P-doping of rGO in the HER electrocatalytic activity of the respective doped and undoped rGO-supported Ru NPs. **Ru@P-rGO** was prepared following the same synthesis protocol as for **Ru@rGO** and **Ru@NH$_2$-rGO** (Scheme 1).[30,33] Thus, the decomposition of [Ru(COD)(COT)] under mild conditions (3 bar H_2, 20 h, RT) over the three supports led to the formation of small Ru NPs. The metal contents of the three materials were determined by ICP-OES, providing in all cases values close to the theoretical one, 3 wt%, *i.e.* **Ru@rGO**: 2.4 wt% Ru; **Ru@NH$_2$-rGO**: 2.5 wt% Ru and **Ru@P-rGO**: 3.1 wt% Ru.

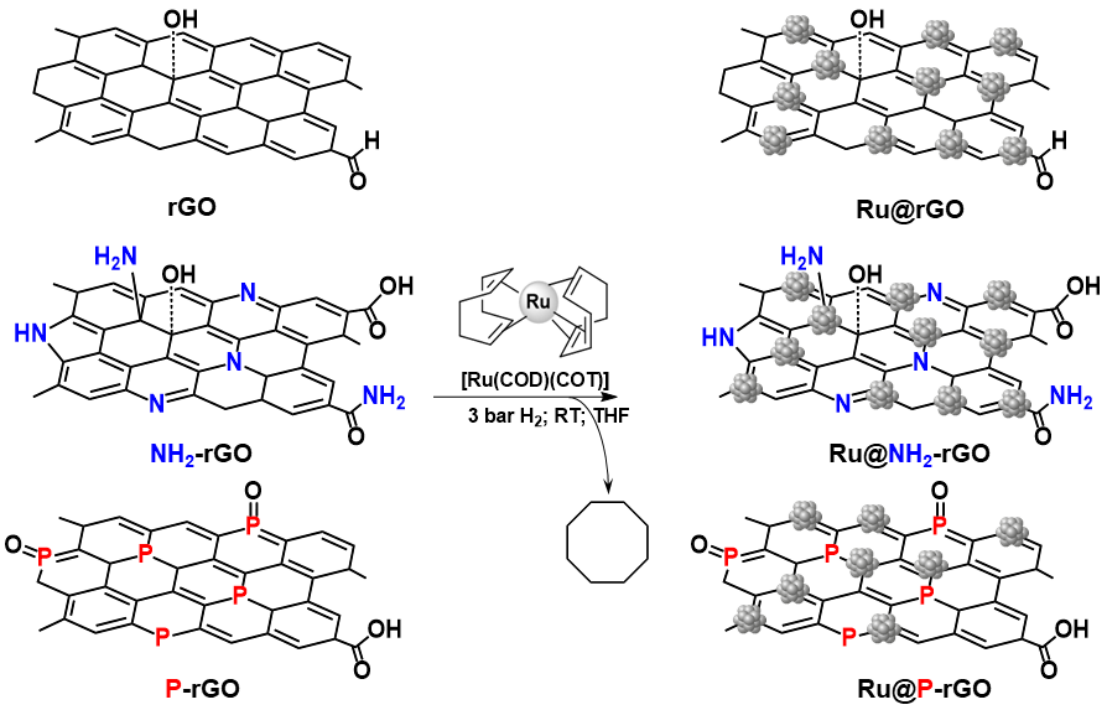

Scheme 1. Synthesis of **Ru@rGO**, **Ru@NH₂-rGO** and **Ru@P-rGO** materials from the [Ru(COD)(COT)] organometallic complex (grey spheres represent Ru atoms).

Transmission electron microscopy (TEM) analyses revealed the formation of small, monodisperse and well-distributed NPs in all cases. **Ru@NH₂-rGO** and **Ru@P-rGO** show the smallest and most homogeneous particle size with a mean diameter of *ca.* 1.5 nm (Figure S1d-i), with low size dispersion (± 0.2 and ± 0.3 nm, respectively) and good distribution onto the carbonaceous support. The undoped rGO material, **Ru@rGO**, presents higher particle mean size and size dispersion (2.0 ± 0.8 nm) and worse distribution than its doped counterparts (Figure S1a-c). These differences in Ru NP size homogeneity and distribution result from the positive effect of the heteroatom doping in the stabilization of Ru NPs and distribution at the rGO surface, as previously observed in similar doped graphene systems.[13,30,34] High resolution TEM (HRTEM) analyses confirmed the crystallinity of the Ru NPs in all cases (Figure S2). As previously observed for **Ru@NH₂-rGO**,[30] the Fourier analysis of the HRTEM image of **Ru@P-**

rGO indicates the presence of a hexagonal close packed (hcp) structure typical for Ru^0 (active species in H_2 dissociation), with reflections due to the (100) and (002) atomic planes (Figure S2c).

P-rGO and **Ru@P-rGO** materials were analyzed by Raman spectroscopy. As in the rGO[34] and NH_2-rGO[30] spectra, the spectrum of P-rGO exhibits two major bands at 1368 cm^{-1} (D peak) and 1592 cm^{-1} (G peak), together with a broad peak around 3000 cm^{-1} (2D peak) (Figure S3a). The high D/G ratio (I_D/I_G = 2.01) is related to the large percentage of defects of this support, which are excellent anchoring points for NP stabilization, as compared to the previously reported I_D/I_G ratios for rGO (1.54)[34] and NH_2-rGO (1.49).[30] The presence of Ru NPs onto P-rGO (**Ru@P-rGO**) leads to a slight decrease in the I_D/I_G ratio down to 1.92 (Figure S3b), indicating a decrease in the number of defects in the P-rGO support due to the preferential growth of Ru NPs over these defects, improving their stability during electrocatalysis (*vide infra*).

The presence/nature of P atoms and the chemical composition of **Ru@P-rGO** were analyzed by X-ray photoelectron spectroscopy (XPS). The C 1s signal of P-rGO shows a peak at a binding energy (BE) of 284.8 eV, that can be deconvoluted into three components (Figure S4c). The main component at 284.8 eV (red) belongs to the sp^2 C atoms of the graphitic domains (~ 77 %), and the two minor contributions are attributed to carbon atoms linked to P or O atoms (287.0 eV; green; ~ 11 %) and to carboxylic groups (289.2 eV; blue; ~ 12 %). C 1s signals of rGO and NH_2-rGO are very similar, with the only difference that the component at ~ 286-287 eV (green) corresponds to carbon atoms of epoxides, tertiary alcohols and/or C atoms connected to N (Figure S4a,b). The presence and nature of P atoms on the P-rGO support were confirmed after analysing the P 2p region (Figure S5a). The P 2p area shows a broad peak which can be

deconvoluted in two contributions, one centered at 133.1 eV (grey), corresponding to P atoms bonded to oxygen atoms (~ 41 %), and another one at 130.9 eV (blue), attributed to P–C bonds (~ 59 %). These peaks have been previously identified in similar P-doped graphenes.[35,36] In the P-rGO case, the percentage of graphitic phosphorus atoms (P–C) is higher than in the P-doped graphene obtained from alginate,[13] where P is mainly in the phosphate (P–O) form. The existence of this minor (~ 41 %) P–O phase in P-rGO indicates that the doped P atoms have been partially oxidized by the oxygen released from GO during the synthetic reductive process. Analysis of the P 2p signal allowed to determine the P content of P-rGO, which is 1.26 at% (2.94 wt%). Also, as previously reported,[30] the N-containing groups present in NH_2-rGO are graphitic, pyridinic, pyrrolic or amino groups, the last two being the most abundant ones.

Moreover, the oxidation state of Ru in **Ru@P-rGO** before and after reduction treatment (180 °C under a H_2 flow for 5 h) was studied by XPS analysis of the Ru 3p region. Figure S5b exhibits the Ru $3p_{3/2}$ area of the as-synthesized **Ru@P-rGO**, where a peak centered at 463.2 eV is observed. The deconvolution of this peak presents two different components, one at 464.4 eV, attributed to Ru(IV) and characteristic of RuO_2, and another one at 462.7 eV, corresponding to Ru(0).[37] These results confirm the formation of a RuO_2 passivation layer around the Ru(0) core after purification of the material in air, as we have otherwise demonstrated in related systems.[12,37] However, after applying reduction conditions, the Ru(0) component at *ca.* 462 eV increases at the expense of that corresponding to RuO_2 (Figure S5c). In the same way, the Ru 3p XPS spectra of **Ru@rGO** and **Ru@NH_2-rGO** show that before reduction treatment most of the Ru is as RuO_2, whereas after the reduction treatment the main component is Ru(0) (Figure S6). Precise amounts of Ru(0) and RuO_2 before and after reduction treatment are shown in Table S1,

indicating higher percentages of Ru(0) after reduction in the doped materials than in the undoped one (48.4 % for **Ru@rGO**, 72.6 % for **Ru@NH_2-rGO** and 87.3 % for **Ru@P-rGO**).

Finally, the nature of the P atoms in P-rGO has also been examined by ^{31}P MAS solid state NMR spectroscopy. The ^{31}P MAS NMR spectrum shows a very broad band centered at 0 ppm (Figure S7). According to the literature, the width of this peak is attributed to a wide array of sites with slightly different isotropic chemical shifts,[4,38] indicating the existence of graphitic phosphorus or oxidized graphitic phosphorus bonded to three sp^2-hybridized carbon atoms, as has also indicated by the XPS studies.[4,38]

The HER electrocatalytic performance of **Ru@rGO**, **Ru@NH_2-rGO** and **Ru@P-rGO** was evaluated in 1 M H_2SO_4 aqueous solution. Working electrodes were prepared by dispersing the materials in THF (2 mg·mL^{-1}) and drop-casting them onto a glassy carbon rotating disk electrode (GC-RDE). The polarization curves and corresponding Tafel plots of **Ru@rGO**, **Ru@NH_2-rGO** and **Ru@P-rGO** are shown in Figure 1 (bold lines). A change in the current density is observed when scanning into reductive potentials, confirming the catalytic reduction of protons into H_2.

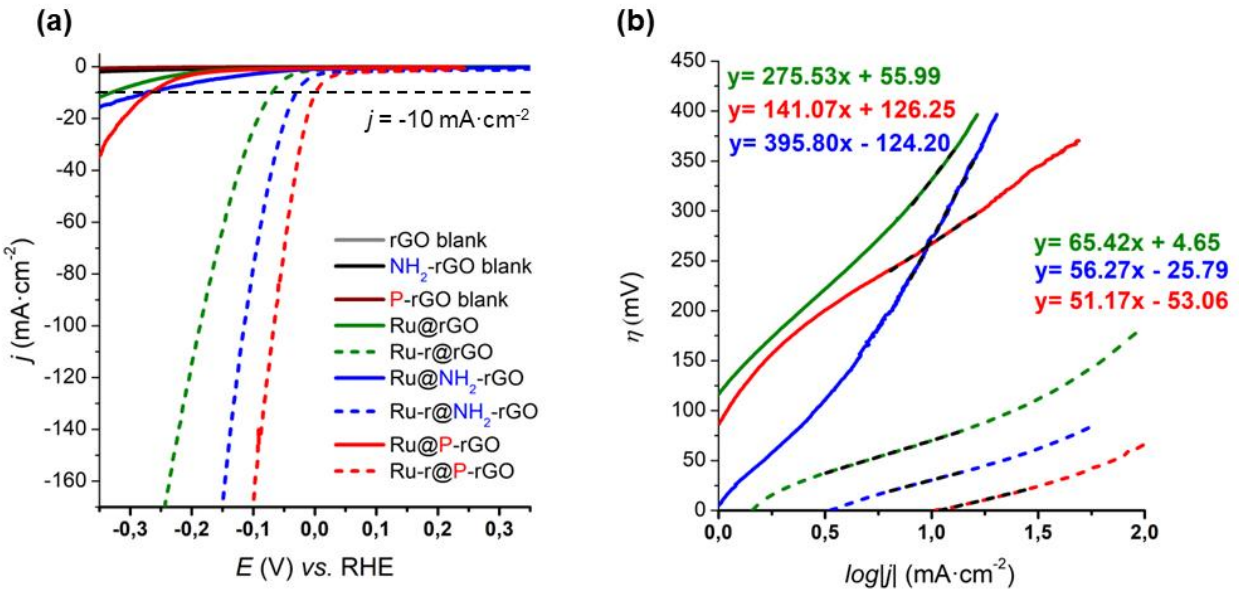

Figure 1. (a) Polarization curves of **Ru@rGO** (green line), **Ru@NH₂-rGO** (blue line) and **Ru@P-rGO** (red line) before (solid) and after (dashed) a 7-15 h reductive process at j = -10 mA·cm^{-2} in 1 M H_2SO_4. rGO (grey line), NH_2-rGO (black line) and P-rGO (wine line) blanks are also shown. (b) Tafel plots of **Ru@rGO**, **Ru-r@rGO**, **Ru@NH₂-rGO**, **Ru-r@NH₂-rGO**, **Ru@P-rGO** and **Ru-r@P-rGO** in 1 M H_2SO_4. Same color code as in (a).

The catalytic performance of the materials can be significantly improved when submitted to a 7-15 h current-controlled bulk electrolysis at j = -10 mA·cm^{-2}. As presented in Figure 1a, whereas **Ru@rGO**, **Ru@NH₂-rGO** and **Ru@P-rGO** show a η_{10} of 331 mV, 274 mV and 268 mV, respectively, a shift in the polarization curves is observed after the reductive process, decreasing the η_{10} down to 71 mV, 30 mV and 2 mV, respectively. This behavior is attributed to a change in the oxidation state of surface Ru atoms on the NPs. As shown by the XPS data (*vide supra*) and our related studies,[12,37] the Ru NPs surface gets partially oxidized (passivated) when exposed to air after their synthesis. When submitted to a reductive potential this RuO_2 passivated surface is reduced back to metallic Ru. Thus, the catalytic current density of the reduced materials, from

now on **Ru-r@rGO**, **Ru-r@NH$_2$-rGO** and **Ru-r@P-rGO**, radically increases in comparison with that of the passivated materials (*i.e.* **Ru@rGO**, **Ru@NH$_2$-rGO** and **Ru@P-rGO**, Figure 1a). We previously performed a deep study of this behavior on 4-phenylpyridine (4-PP) capped[37] and carbon nanotubes- supported Ru (Ru/RuO$_2$) NPs.[12] In both cases, a total disappearance of the RuO$_2$ peak in the XPS was observed, indicating the reduction of the superficial Ru(IV) into Ru(0) under reductive electrochemical catalytic conditions, which can be seen as an activation step.

The different electrocatalytic performance of the as-synthesized/activated **Ru@rGO**/**Ru-r@rGO**, **Ru@NH$_2$-rGO**/**Ru-r@NH$_2$-rGO** and **Ru@P-rGO**/**Ru-r@P-rGO** samples is evidenced from their corresponding Tafel plots (Figure 1b). **Ru-r@rGO** shows a lower Tafel slope of 65 mV·dec^{-1} compared to 276 mV·dec^{-1} for **Ru@rGO**. The same tendency is observed with the heteroatom-doped materials, with **Ru-r@NH$_2$-rGO** showing a slope of 56 mV·dec^{-1} *vs.* 396 mV·dec^{-1} for **Ru@NH$_2$-rGO**, and **Ru-r@P-rGO** a slope of 51 mV·dec^{-1} *vs.* 141 mV·dec^{-1} for **Ru@P-rGO**, as expected for the presence of Ru(0) species in the activated materials by bulk electrolysis. A positive effect of the N- and P-doping rGO supports is also observed in the HER catalytic activity. **Ru-r@NH$_2$-rGO** and specially **Ru-r@P-rGO** show lower overpotentials and Tafel slopes than their bare counterpart **Ru-r@rGO**, and represent some of the best Ru-based HER electrocatalysts reported so far in the literature (see Table S2). As a matter of fact, our activated P-doped material shows the lowest η_{10} value reported until now (only 2 mV).

The Tafel slope (*b*) allows defining the rate determining step (rds) of the HER. **Ru-r@rGO**, **Ru-r@NH$_2$-rGO** and **Ru-r@P-rGO** show slopes of 65, 56 and 51 mV·dec^{-1}, respectively (Figure 1b), suggesting that the HER follows a mechanism in between the Volmer and Heyrovsky steps as rds. In contrast, **Ru@P-rGO** shows a Tafel slope close to 120 mV, typically attributed to the

Volmer step (adsorption of H^+ to form the M–H species) as the rds, whereas **Ru@rGO** and **Ru@NH₂-rGO** show very big Tafel slopes, suggesting an extremely slow H^+ adsorption step related to the presence of a poor catalytically-active RuO_2 shell in the as-prepared samples.

The fate of the materials after short term stability tests (2 h) was assessed by TEM analysis. After 2 h under catalytic conditions at a constant *j* of -10 $mA \cdot cm^{-2}$, each drop-casted material was recovered from the GC-RDE with THF and sonication. Then, a drop of the THF suspension of the recovered material was deposited onto a carbon-coated copper TEM grid. As shown in Figure S8, the mean size of the Ru NPs significantly increased for **Ru@rGO**, while it was similar for **Ru@NH₂-rGO** and **Ru@P-rGO** compared to the corresponding initial materials. These results support the hypothesis that heteroatoms (*i.e.* N or P) stabilize Ru NPs from aggregation/coalescence both during the synthetic process (due to the high number of defects present in the NH_2-rGO and specially the P-rGO surface according to Raman spectroscopy, *vide supra*) and under electrocatalytic conditions.

Long-term stability is a key parameter for a HER electrocatalyst to attain practical use. Thus, once activated, the **Ru-r@rGO**, **Ru-r@NH₂-rGO** and **Ru-r@P-rGO** electrodes were held at a constant current density of $j = -10\ mA \cdot cm^{-2}$ in a current controlled experiment (*i.e.* chronopotentiometry) for 12 h, monitoring the change in the required overpotentials (Figure S9). LSVs before and after the 12 h experiments were also performed and are also shown in Figure S9. The **Ru-r@NH₂-rGO** and **Ru-r@P-rGO** materials show almost no change in η_{10} and almost identical LSV polarization curves before and after electrocatalytic turnover (Figure S9b and S9c). For **Ru-r@rGO**, the stability is also confirmed, obtaining similar performance after 12 h under catalytic turnover. Therefore, even if **Ru@rGO** suffers aggregation and coalescence of Ru NPs during the activation process (see TEM images after 2 h in Figure S8), the resulting **Ru-**

r@rGO nanomaterial presents stable HER electroactivity for at least 12 h. Altogether, the elevated stability of the three supported systems upon uninterrupted catalytic turnover conditions may be related to the strong coordination energies of these Ru NPs onto the supports (see DFT calculations below). Also, faradaic efficiencies of 96-98% were determined by quantifying the amount of H_2 generated during a 20 min chronoamperometry using a H_2-Clark electrode and comparing it with the maximum theoretical amount of H_2 calculated from the total charge passed through the electrode (Figure S10). This confirms the production of H_2 as the sole reaction occurring with all materials studied.

A final comparison of the main physicochemical and electrocatalytic data for the three studied materials is shown in Table 1, including the calculation of the exchange current density (j_0) for all and of the cathodic transfer coefficient (α) for the activated materials only (Figure S11). These data will be discussed and used for the theoretical modelling (*vide infra*).

Table 1. Summary of physicochemical and HER electrocatalytic data for the materials studied (1 M H_2SO_4 aqueous solution at pH 0). Parameters: mean diameter (d_{mean}) before (t=0) and after (t= 2h) catalysis, onset overpotential at -10 $mA \cdot cm^{-2}$ (η_{10}), Tafel slope (b), exchange current density (j_0) and cathodic transfer coefficient (α).

Entry	System	d_{mean} t=0 (nm)	d_{mean} t=2h (nm)	Ru (wt.%)	η_{10} (mV)	b ($mV \cdot dec^{-1}$)	j_0 ($mA \cdot cm^{-2}$)	α
1	Ru@rGO	2.0 ± 0.8	4.3 ± 0.9	2.4	331	276	0.63	-
2	Ru-r@rGO	-	-	-	71	65	0.85	0.39
3	Ru@NH_2-rGO	1.5 ± 0.2	1.9 ± 0.23	2.5	274	396	2.06	-
4	Ru-r@NH_2-rGO	-	-	-	30	56	2.87	0.45
5	Ru@P-rGO	1.5 ± 0.3	1.4 ± 0.2	3.1	268	141	0.13	-

6	Ru-r@P-rGO	-	-	-	2	51	10.88	0.50

As discussed above, the activation of the materials provokes a concomitant decrease of the Tafel slope (*b*) and of the η_{10} value for all three materials, especially for the P-doped one, yielding a η_{10} value as low as 2 mV. Concerning the j_0 value, it increases moderately for the rGO and NH_2-rGO supports upon activation (ca. 35-40%), and dramatically for P-rGO (more than 80 times), reaching up to 10.88 $mA \cdot cm^{-2}$. Thus, the tendency of all electrochemical parameters clearly points to a **Ru-r@rGO** < **Ru-r@NH_2-rGO** < **Ru-r@P-rGO** trend in HER performance.

Finally, the electrochemically active surface area (ECSA) for the non-activated materials **Ru@rGO**, **Ru@NH_2-rGO** and **Ru@P-rGO** has been assessed (Figure S12), obtaining very similar values for all materials (5.9, 4.0 and 2.9 cm^2, respectively), in contrast to previous results obtained for related alginate derived graphene,[13] where the incorporation of P into the carbon structure made the final material more exfoliated and less rough. The similarity in ECSA of the three materials before activation here studied indicates that the differences observed among the three activated systems may not be due to a significant difference in the number of active sites, but to different intrinsic catalytic activities of the catalytic sites on each support. To further confirm this hypothesis, DFT calculations have been performed as follows.

After having characterized the electrocatalytic behavior of the three rGO-supported Ru materials, and in view of the already-known respective electron acceptor and electron donor effects of N and P atoms adjacent to C atoms in graphitic structures,[5] the electronic effects of these doping-heteroatoms in the materials have been addressed by a thorough DFT theoretical approach. The presence of the heteroatoms could endeavour a concomitant effect in the electronic structure of

the supported Ru NPs, thus provoking a synergistic effect between the Ru NPs and the doped-rGO supports, modulating the adsorption energy of reaction intermediates to enhance the HER catalytic activity of the Ru NPs. To this end, the three supports have been modelled by AIMD simulations after considering their experimental EA, XPS and Raman data, following the design procedure of Navarro-Ruiz *et al*.[39] Details are given in section 3.4.1 and Figures S13 and S14 of the SI. In short, it consists in accommodating experimentally proven structural defects, performing a sequence of serial optimizations on the defective graphene, and functionalizing the carbon surface, starting with those found within the carbon lattice, followed by increasingly larger groups. 10 ps AIMD simulations have been made to probe the thermal stability of these functionalized surfaces, reached after approximately 5 ps. The final geometry of the simulation is then relaxed by a local geometry optimization. The moderate concentration of oxygenated groups induces a loss of planarity of rGO, giving rise to the formation of remarkable superficial corrugations. The N-doped support presents a higher density of functionalities and, therefore, a higher deformation of the carbon surface. It is worth to mention the increase in vacancy defects on the carbon lattice due to the presence of pyridine and pyrrole rings, including some protonated ones. Functionalization is the least significant on the P-rGO support, partly due to the low P incorporation in the graphene oxide. This leads to a higher concentration of pristine graphitic areas and therefore less rippling of the carbon system. After the support design, DFT calculations (d-band center and charge analysis, ΔG_{H^*} determination) have been performed with two different Ru NP models to analyse the variables that may affect the electrochemical HER activity of the supported Ru NPs, such as the distance of the Ru atoms to the support or the hydride content of the NPs surface.

The two molecular models that have been considered are the two previously published $Ru_{55}H_{53}$ and $Ru_{55}H_{70}$ models,[40] each of them being adsorbed onto the rGO, NH_2-rGO and P-rGO supports obtained after AIMD simulations (Figure 2 and Figure S15). Coordination energies of the $Ru_{55}H_n$ NPs reported in this figure (red numbers, in kcal·mol^{-1}) correspond to the reaction $Ru_{55}H_n$ + substrate -> $Ru_{55}H_n$* (given the in-situ growth of these NPs, the $Ru_{55}H_n$ reactant geometry is the relaxed geometry of its $Ru_{55}H_n$* counterpart, *i.e.* with no hydrides lying at their bottom). All Ru NPs are strongly bound to the support, in the order NH_2-rGO > rGO > P-rGO. Also, we can see that superficial hydrides have a destabilizing effect on the coordination energies of the Ru NPs onto the supports, since they are less strongly attached when their hydride content increases.

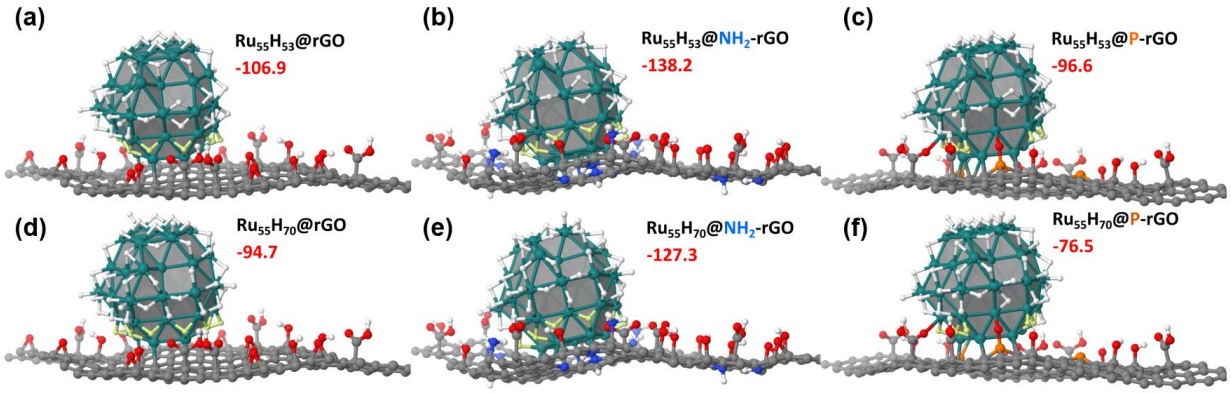

Figure 2. Side views of $Ru_{55}H_{53}$ and $Ru_{55}H_{70}$ NPs on the rGO (a, d), NH_2-rGO (b, e) and P-rGO (c, f) functionalized supports (top views are given in Figure S15). Atomic color scheme: Ru (Green); P (Orange); O (Red); N (Blue); C (Gray); H (White). Grey surfaces highlight the faceting of the Ru_{55} hcp sphere. Yellow hydrogen atoms belong to the [0:3] Å domain, whose HER activity is discussed hereafter. The coordination energy of the $Ru_{55}H_n$ NP is also given in each case, in kcal·mol^{-1} (red numbers).

The effect of each of the three supports on the electronic structure of the bare Ru_{55} model has been first evaluated to assess the intrinsic effect of the support on the electronic structure of the metallic Ru. It also provides clues about the adsorption strength of hydrides at the Ru NP surface, under the possible influence of the support. Yet, such bare NPs would tend to maximize their interaction with the support to compensate for the lack of stabilizing effect of surface hydrides. Besides, the geometry optimization leads to a significant increase of the interaction between some surface species of the rGO supports that is not representative of the actual interaction of these supports with hydrogenated Ru NPs. Therefore, this preliminary analysis was carried out on the $Ru_{55}H_{70}$@X frozen geometry, from which the 70 hydrides have been removed (X = rGO, NH_2-rGO, P-rGO). After projection of the PAW wavefunctions into an auxiliary LCAO basis set by the Lobster software (see DFT computational details section in the SI), it is possible to calculate d-band centers[41] and Mulliken-like population analysis (MPA).[42] Results are summarized in Figure 3 (a detailed description of the values commented hereafter is given in the caption), in which the Ru NPs are discretized in a series of five parallel close-packed planes (cpp) numbered from 1 to 5, with cpp1 corresponding to the layer in contact with the support and cpp5 the outermost layer from the support (see Figure S19 for a detailed description). Regarding the supports, unfunctionalized carbon atoms are in general neutral, whilst the functionalization involves small local charge transfer, as otherwise observed for small hydrogenated Pd NPs deposited on graphene-derived substrates.[39]

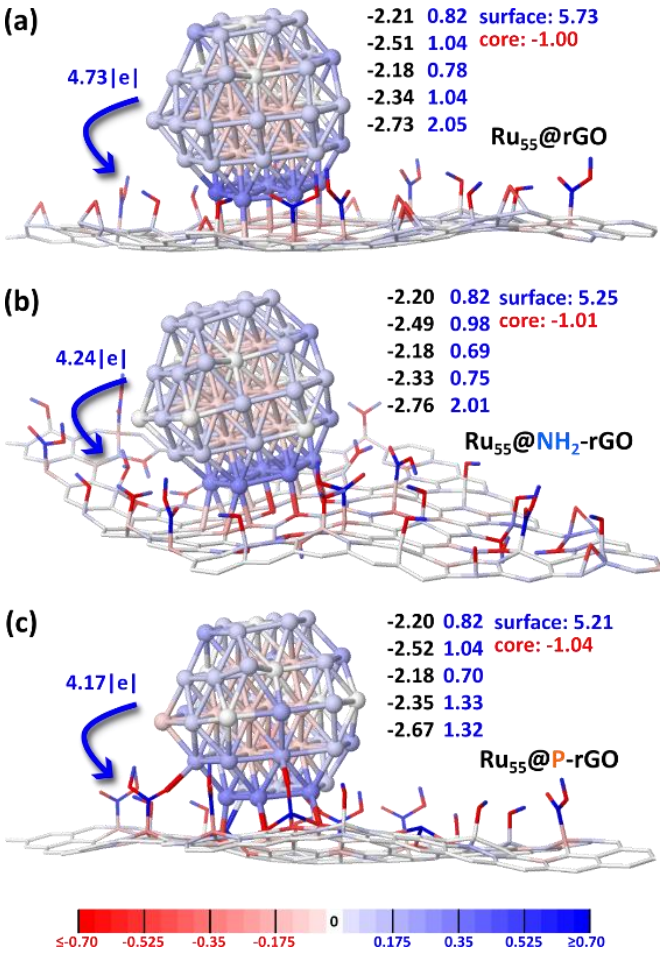

Figure 3. d-band center and MPA charge analysis of Ru_{55}@rGO (a), Ru_{55}@NH_2-rGO (b) and Ru_{55}@P-rGO (c). Atom colors correspond to their electronic charge, according to the scale plotted at the bottom of the figure. rGO supports are plotted as wireframes to better see Ru atomic charges. The number above each blue arrow is the charge transfer from the Ru_{55} model to the support. The two-column numbers for each system are the average d-band center (left, in black) and the total charge (right, in blue) calculated for the surface Ru atoms of each of the five close-packed planes (cpp) from cpp1 (bottom) to cpp5 (top) (see Figure S19 for a detailed description). Pay attention that the total charge of core Ru atoms is slightly negative (red numbers). The charge of surface atoms is also given.

The striking feature is the oxidation of the Ru_{55} model by all the supports, with a significantly stronger charge transfer induced by the rGO support (4.73|*e*| *vs*. NH_2-rGO, 4.24 |*e*|, and P-rGO, 4.17|*e*|). The surface atoms of the close-packed plane (cpp) close to the support, cpp1, are in general more strongly oxidized than the other surface atoms (darker blue atoms and blue values at the column bottom in Figure 3). Whereas the MPA charge of cpp1 is ca. 2|*e*| for Ru_{55}@rGO and Ru_{55}@NH_2-rGO, it is only 1.3|*e*| in Ru_{55}@P-rGO. The reason probably lies in the direct interaction of surface species with one surface Ru atom of cpp2. The overall charge of surface atoms of cpp1 and cpp2 is similar between Ru_{55}@NH_2-rGO and Ru_{55}@P-rGO (2.76|e| and 2.65|e|) and lower than the one calculated in the Ru_{55}@rGO model (3.09|e|). These local charges as well as the NP-to-support charge transfer are noticeable different features between Ru_{55}@rGO on one hand and Ru_{55}@NH_2-rGO and Ru_{55}@P-rGO on the other hand. Incidentally, they do not vary in the same order as the coordination energies of the $Ru_{55}H_n$ NPs (Figure 2) and thus there seems not to be any relationship between the coordination energy of the Ru NPs onto the supports and the charge transfer processes taking place between them.

The d-band centers, ε_d, of the surface atoms of the cpp planes are also reported in black in Figure 3. ε_d calculated for the cpp1 surface atoms (-2.73 eV, -2.76 eV, -2.67 eV) lie farther away from the Fermi energy level than the other cpps, in line with the stabilization of these atoms by the direct interaction with the support. The other values are closer to the Fermi energy band, and there is virtually no difference between the three models. The fact that the d-band center of cpp2 to cpp5 lie close to the Fermi level means that oxygen atoms will adsorb very strongly once these NPs are put in contact with air, pointing that the RuO_2 passivation layer will be highly stable and thus difficult to be removed by electrochemical reduction (Figure 1, bold lines). This would explain why very long electrochemical activation times (7-15 h) are needed to fully activate the

rGO-supported Ru NPs (Figure 1, dashes lines), in contrast to their 4-phenylpyridine (4-PP) capped counterparts,[37] which become completely active in HER electrocatalysis after a short 20-min activation time. On the other hand, the only significant difference in the Ru_{55}@P-rGO model compared to the other two models is the d-band center of the cpp1 surface atoms, which is closer to the Fermi level by 0.06 eV and 0.09 eV with respect to Ru_{55}@rGO and Ru_{55}@NH_2-rGO, respectively. This suggests, given the usual interpretation of the d-band center descriptor, that this part of the surface will be slightly more reactive in Ru_{55}@P-rGO. These data, together with a lower Ru NP-to-support charge transfer in this system as well as in Ru_{55}@NH_2-rGO (4.17|e| and 4.24|e|, compared to 4.73|e| in Ru_{55}@rGO), indicate that a difference in the catalytic activity of the Ru surface can be expected between the three supported Ru NPs. This is what is now going to be assessed differently by calculating hydrogen adsorption free energies, ΔG_{H^*}**,** of all hydrides present at the surface of the Ru NPs as a function of their distance to the support surface (see section 3.6 of the SI for further details). As explained in section 3.5 of the SI, each ΔG_{H^*} value can be easily correlated with the theoretical exchange current density value (j) corresponding to each reactive site, obtaining the so-called volcano plots.

To compute the dependence of ΔG_{H^*} *vs.* the exchange current density we have used the experimental cathodic transfer coefficient values (α values) and the recently improved Yang and Saidi model[31,32] instead of the most frequently used (and less realistic in the more strongly adsorbed hydride regime) Nørskov model[21,22] (see section 3.5 of the SI, Figs. S16-S18 and Table S3 for further details). Then, the theoretical ΔG_{H^*} values were calculated for all sites at a distance *R* from the support (see section 3.6 of the SI for more information), and the corresponding volcano plots were generated considering the overall effect of all hydrides present on the Ru NPs (Figure 4a) or only the ones at a distance *R* below 3 Å (Figure 4b). Furthermore, two different Ru

NP models, namely $Ru_{55}H_{53}$ (1.2 H^- per surface Ru atom, Figure 4, top) and $Ru_{55}H_{70}$ (1.6 H^- per surface Ru atom, Figure 4, bottom), were considered. The *ca.* 1.2:1 surface composition is usually measured for unsupported, ligand-protected, Ru NPs.[43] Yet, in a previous DFT-*ab initio* thermodynamics study carried out on the same Ru_{55} model without any surface ligands, 1.6:1 was found to be the optimal hydride-to-surface Ru atom ratio at RT and up to 350 K for a pressure of 1 bar of H_2.[44] This ratio might be more representative of a supported Ru NP, where only a rather small part of the surface is stabilized, although it is by a polycyclic support that strongly binds it (Figure 2). In Figure 4a, all 53 or 70 hydrides are accounted for, leading to the calculation of what has been defined as $\overline{\log \hat{\jmath}_0(R_{\max})}$. In Figure 4b, only hydrides at distances below 3 Å from the support surface (shown in yellow in Figure 2) are considered, thus yielding what has been defined as $\overline{\log \hat{\jmath}_0(3)}$. For the latter, they represent 12 to 15 % of the total number of hydrides, and they are bound to Ru atoms under the direct influence of the support, *i.e.* Ru atoms that belong to the cpp1 layer. Thus, these are bridging H atoms between the cpp1 and cpp2 layers.

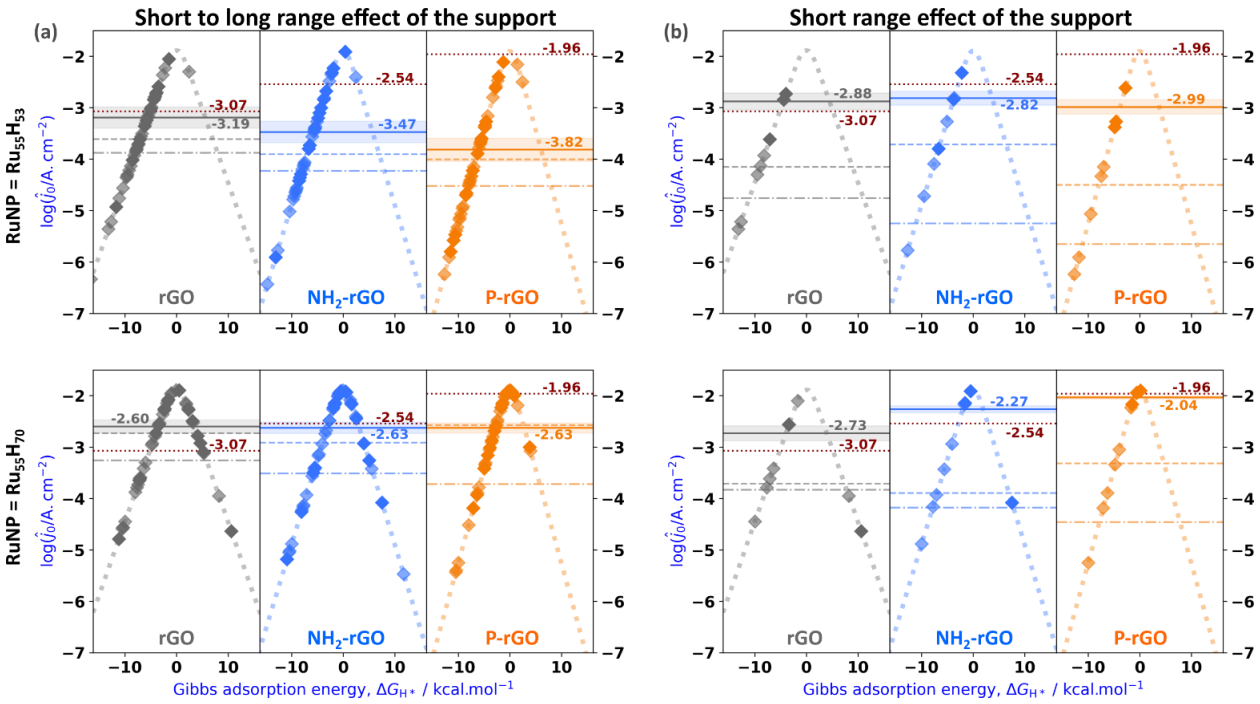

Figure 4. Effect of the support on $\overline{\log \hat{j}_0(R_I)}$ and on $\log \hat{j}_0$ calculated in each [R_i, R_{i+1}] interval: (a) short to long range effect ($R \leq R_{max}$, see Figure S19); (b) short range effect ($R \leq 3$ Å). Calculations done on the $Ru_{55}H_{53}$ and $Ru_{55}H_{70}$ models are reported on the upper or lower part of each subfigure, respectively. The slope of each volcano depends on the experimentally measured α value. This figure shares some conventions with Figure S20: the experimental $\log j_0$ value is reported in as a horizontal dotted claret line; dark color diamonds: $\log \hat{j}_0$ values calculated for the supported $Ru_{55}H_n$ model in each [R_i, R_{i+1}] interval, between $R_0 = 0$ and $R_I = R_{max}$ (a) or $R_I = 3$ Å (b); light color diamonds: $\log \hat{j}_0$ values calculated for the same intervals, but on the unsupported $Ru_{55}H_n$ model; the corresponding $\overline{\log \hat{j}_0(R_I)}$ averaged value is also reported in both cases, just above or below horizontal grey, blue or orange plain lines; dashed lines show results obtained for the unsupported $Ru_{55}H_n$ model in the same geometry as in the supported system, *i.e.* with no hydrides in the grafting domain of the NP (labelled '$Ru_{55}H_n$@X-rGO after supp. system' in Figure S20); dash-dotted lines

show $\overline{\log \hat{j}_0(R_I)}$ calculated on the original $Ru_{55}H_n$ models developed in ref. 44, *i.e.* with hydrides distributed on the whole surface of the Ru_{55} model (labelled '$Ru_{55}H_n$ eq.' in Figure S20).

Before comparing the theoretical outcome with the experimental data, a few general characteristics that could be responsible for the differences in the calculated exchange current densities will be reviewed:

(i) Effect of the increase of the number of surface hydrides per unit area on j_0. As explained in section 3.6 of the SI and in Figure S20, the dash-dotted horizontal lines in Figure 4 correspond to the predicted $\log \hat{j}_0$ exchange current densities calculated for the hydride sites distributed on the whole Ru surface on unsupported Ru NPs, while the dashed horizontal lines refer to the $Ru_{55}H_n$ model after being supported onto the different x-rGO. It differs from the previous $Ru_{55}H_n$ model in the reduced surface area occupied by the hydrides, since the lower part of the NP interacts with the support. It can be almost systematically observed that in this case, the H---H repulsive interaction weakens their adsorption energy, resulting in an increase of the exchange current density. Provided that rGO surfaces do not involve a significant change in the Ru NP surface composition, the increased number of surface hydrides per unit area could explain in part the differences in electrocatalytic activity between supported and unsupported Ru NPs.

(ii) *The support has a short-range influence only*. Given the volcano plots determined for $\overline{\log \hat{j}_0(R_{\max})}$ in Figure 4a, the effect of the support is quite small when compared to the unsupported models. There is a moderate increase in the exchange current density, whereas it is much greater when we inspect the short-range effect (below 3 Å) of the graphene surfaces in Figure 4b. This can be understood by examining the diamond symbols reported on the volcano plots, where the dark colors correspond to the hydrides belonging to supported Ru NPs, whereas

the light colors correspond to hydrides belonging to unsupported Ru NPs. Most of the dark color diamonds lie quite close to the top in Figure 4b, while most of the light diamonds lie further away from the top. Thus, the adsorption strength of hydrides close to the support is in general small to moderate. In contrast, Figure 4a reveals that most of the hydrides lay on the slopes of the volcanos, both for the supported and the unsupported cases, with no significant differences amongst them. Thus, they are strongly adsorbed (ΔG_{H^*} < -5 kcal·mol^{-1}), especially when considering the $Ru_{55}H_{53}$ model (Figure 4a, top). Consequently, $\overline{\log \hat{j}_0(3)}$ is usually less negative than $\overline{\log \hat{j}_0(R_{max})}$, with the only exception of $Ru_{55}H_{70}$@rGO, for which the two predicted values are very close (-2.73 *vs*. -2.60). In other words, the support acts locally as a macrocyclic ligand which increases the HER catalytic activity of its neighboring Ru atoms only by decreasing the ΔG_{H^*} values.

(iii) *A synergy of effects*. If we now focus on Figure 4b, in order to discuss the intrinsic effect of the surface on ΔG_{H^*} and by consequence on $\log \hat{j}_0$, this effect, combined with the H---H repulsive interaction discussed in (i), tends to bring $\log \hat{j}_0$ close to the top of the volcano (~ -2), a criterion of strong HER activity for the corresponding catalysts ($Ru_{55}H_{53}$@X: -2.88, -2.82, -2.99; $Ru_{55}H_{70}$@X: -2.73, -2.27, -2.04, with X = rGO, NH_2-rGO, P-rGO, respectively). The intrinsic effect of the support is strong when compared with the unsupported $Ru_{55}H_n$ models, with an increase of $\overline{\log \hat{j}_0(3)}$ for $Ru_{55}H_{53}$@X of +1.27, +0.90, +1.51, as well as for $Ru_{55}H_{70}$@X of +0.98, +1.64, +1.28 (these are the differences between plain lines and dashed lines in Figure 4b, with X = rGO, NH_2-rGO, P-rGO, respectively).

Finally, we will determine which model best agrees with the experimental measurements. If we now go back to the experimental HER activity of the three studied materials, it decreases in the

order **Ru-r@P-rGO** (log $\hat{j}_0$: -1.96) > **Ru-r@NH$_2$-rGO** (log $\hat{j}_0$: -2.54) > **Ru-r@rGO** (log $\hat{j}_0$: -3.07) (horizontal dotted claret lines in Figure 4). Can the DFT-based simulations explain this trend? If we analyse the overall effect of the support on log j0 given by the calculation of $\overline{\log \hat{j}_0(R_{\max})}$ (Figure 4a) and compare it with the experimentally measured values, we can see in that $\overline{\log \hat{j}_0(R_{\max})}$ does not follow the experimental trend for the grafted $Ru_{55}H_{53}$ model. A fair agreement is observed between theory and experiment for **Ru-r@rGO** (-3.19 *vs.* -3.07), but there is a strong disagreement for **Ru-r@NH$_2$-rGO** (-3.47 *vs.* -2.54) and an even worse discrepancy for **Ru-r@P-rGO** (-3.82 *vs*. -1.96). Concerning the $Ru_{55}H_{70}$ model, the predicted $\overline{\log \hat{j}_0(R_{\max})}$ values are in better agreement, although the experimental trend is not obtained since the exchange current is predicted to be almost the same between the three $Ru_{55}H_{70}$ supported models ($\log \hat{j}_0$: -2.60, -2.63 and -2.63), in contrast with the progressive increase of the exchange current density observed in the experiments between **Ru-r@rGO**, **Ru-r@NH$_2$-rGO** and **Ru-r@P-rGO**, respectively. Thus, the results plotted in Figure 4a do not follow the experimental trend nor the expectations from the electronic structure analysis, particularly the possible higher activity of **Ru-r@P-rGO** according to its d-band center value. This is just an apparent contradiction, given that all the Ru NPs surface site activities are averaged in $\overline{\log \hat{j}_0(R_{\max})}$, even those that are opposite to the support, and therefore not sensitive to the effect of the graphene-derived support. However, this is not the case for the 12 to 15% of hydrides accounted for in the calculation of $\overline{\log \hat{j}_0(3)}$ (Figure 4b). With -2.88, the predicted value is reasonably close to the experimental value (-3.07) for $Ru_{55}H_{53}$@rGO. The agreement is less convincing for the other materials, with a moderate underestimation for $Ru_{55}H_{53}$@NH_2-rGO (-2.82 instead of -2.54) and a strong underestimation for $Ru_{55}H_{53}$@P-rGO (-2.99 instead of -1.96). The resulting computed trend, $Ru_{55}H_{53}$@P-rGO < $Ru_{55}H_{53}$@rGO < $Ru_{55}H_{53}$@NH_2-rGO is not in line with the

experiments. In contrast, the experimental trend is achieved by the $Ru_{55}H_{70}$ model. Although $\overline{\log \hat{j}_0(3)}$ is a bit overestimated for $Ru_{55}H_{70}$@rGO (-2.73 vs. -3.07) and $Ru_{55}H_{70}$@NH_2-rGO (-2.27 vs. -2.54) and slightly underestimated for $Ru_{55}H_{70}$@P-rGO (-2.04 vs. -1.96), the predicted values follow the very same experimental relative activity values trend, the best catalyst for HER being $Ru_{55}H_{70}$@P-rGO, followed by $Ru_{55}H_{70}$@NH_2-rGO and finally $Ru_{55}H_{70}$@rGO. Given the wealth of experimental and theoretical knowledge we have on small Ru NPs,[44] it is reasonable to consider that their surface can accommodate at least 1.5 H^- per surface ruthenium atom when stabilized by a single macrocycle-like ligand.

CONCLUSIONS

In this work, we have studied the effect of N- and P-doping of rGO onto the electrocatalytic activity of the respective supported Ru NPs, observing an outstanding activity (η_{10} of only 2 mV) for the P-doped material. Owing to a thorough modelling of the supports and an accurate DFT analysis of the rGO-supported Ru NPs, a consistent trend between computed and experimental exchange current densities have been obtained. This has involved being accurate enough to reproduce small variations of the average hydrogen adsorption free energy descriptor, ΔG_{H^*}. Furthermore, theoretical DFT calculations have shown to be an alternative and reliable way to estimate the amount of surface hydrides in Ru NPs when supported onto heterogeneous surfaces such as doped-rGO, conditions where the experimental titration of hydrides by reaction with 2-norbornene[45] is not practical nor feasible. A good agreement between theory and experiments has been found with a $Ru_{55}H_{70}$ model, *i.e.*, a model containing 1.6 H^-/Ru_{surf}, but only on the assumption that the observed experimental activity of Ru NPs arises solely from the Ru atoms close to the graphene-derived support (below 3 Å), which are generally the more active ones.

Moreover, in this scenario we should not discard the possibility that some Ru NPs may be in contact with the support through more than one ccp layer, that is, that some NPs were somehow embedded in the carbonaceous support. This would increase the number of high activity sites and thus the overall HER electrochemical capacity of the whole material. Unfortunately, it is not in our hands to experimentally determine the real number of ccps that are in contact with the rGO surfaces. In any case, the resulting calculated exchange current density, j_0, which is a measure of the efficiency of the catalyst with respect to HER, seems to be related to a combination of several parameters: the high d-band center of Ru atoms coordinated to the substrate, the weaker charge transfer between Ru NPs and the support, and a sufficiently high hydride coverage that slightly destabilizes surface hydrides through increased H---H repulsions.

In this work both the experimental and theoretical results converge and confirm the positive synergistic effect between the heteroatoms (especially P) and the Ru NPs to obtain excellent HER electrocatalytic activities. This work paves the way for a better understanding of the intricate interrelated factors determining the HER electrocatalytic activity of supported Ru NPs in heteroatom-doped rGO surfaces, thus opening new avenues for improved designs of superior HER electrocatalysis.

ASSOCIATED CONTENT

Supporting Information. Materials & Methods, Microscopy images, Raman data, XPS data, NMR data, LSV data, bulk electrolysis data, electrochemical parameters determination, relevant related literature data, and DFT computational details (PDF).

AUTHOR INFORMATION

Corresponding Authors

Roger Bofill, Xavier Sala: Departament de Química, Universitat Autònoma de Barcelona, 08193 Bellaterra (Catalonia), Spain. E-mail: Roger.Bofill@uab.cat; Xavier.Sala@uab.cat

Romuald Poteau: Université de Toulouse; INSA, UPS, CNRS; LPCNO (IRSAMC), 135 avenue de Rangueil, F-31077 Toulouse, France. E-mail: romuald.poteau@insa-toulouse.fr

Luis Miguel Martínez-Prieto: ITQ, Instituto de Tecnología Química (CSIC-Universitat Politècnica de València), Av. de los Naranjos S/N 46022, Valencia, Spain & IIQ, Instituto de Investigaciones Químicas (CSIC-Universidad de Sevilla), Avda. Américo Vespucio 49, 41092 Seville, Spain. E-mail: luismiguel.martinez@csic.es

Karine Philippot: CNRS, LCC (Laboratoire de Chimie de Coordination), UPR8241, Université de Toulouse, UPS, INPT, Toulouse cedex 4 F-31077, France. E-mail : Karine.Philippot@lcc-toulouse.fr

Author Contributions

The manuscript was written through contributions of all authors. All authors have given approval to the final version of the manuscript. ‡These authors contributed equally.

Notes

The authors declare no competing financial interest.

ACKNOWLEDGMENTS

X.S. thanks ICREA for the ICREA Academia Prize 2020. X.S. and J.G.-A. thank MINECO/FEDER (PID2019-104171RB-I00) and MICINN (PID2023-146787OB-I00). L.M.M.P also acknowledges the Junta de Andalucía (ProyExcel_00706) for financial support, as well as Grants PID2021-126080OA-I00, TED2021-132087A-I00 and CNS2023-145078 funded by MICIU/AEI/ 10.13039/501100011033 and by "ERDF/EU" and "European Union NextGenerationEU/PRTR. L.M. thanks the UAB for a PhD grant. J.N.R., I.dR. and R.P. thank the CALMIP HCP for generous allocation of computational time (grant P0611). N.R. and K.P. thank CNRS and University of Toulouse 3 - Paul Sabatier for financial support.

TOC:

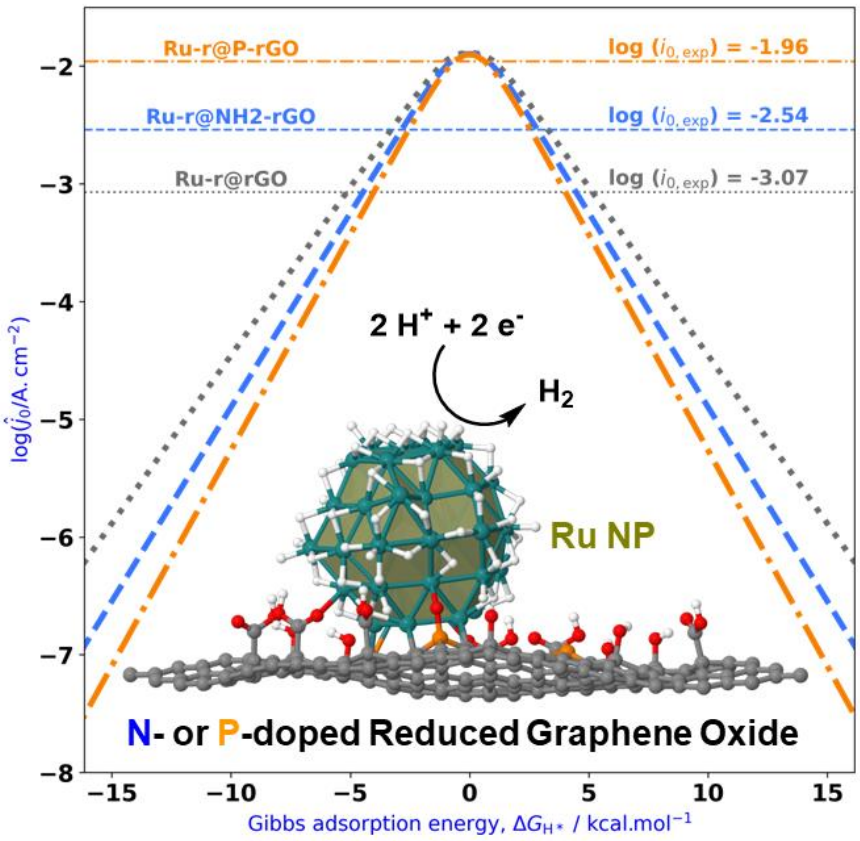

REFERENCES

[1] Martí, G.; Mallón, L.; Romero, N.; Francàs, L.; Bofill, R.; Philippot, K.; García-Antón, J.; Sala, X. Surface-Functionalized Nanoparticles as Catalysts for Artificial Photosynthesis. *Adv. Energy Mater.* **2023**, No. 2300282. DOI: 10.1002/aenm.202300282

[2] Liang, Y.; Li, Y.; Wang, H.; Dai, H. Strongly Coupled Inorganic/Nanocarbon Hybrid Materials for Advanced Electrocatalysis. *J. Am. Chem. Soc.* **2013**, *135* (6), 2013–2036. DOI: 10.1021/ja3089923

[3] Lai, L.; Chen, L.; Zhan, D.; Sun, L.; Liu, J.; Lim, S. H.; Poh, C. K.; Shen, Z.; Lin, J. One-Step Synthesis of NH_2-Graphene from in Situ Graphene-Oxide Reduction and Its Improved Electrochemical Properties. *Carbon* **2011**, *49* (10), 3250–3257. DOI: 10.1016/j.carbon.2011.03.051

[4] MacIntosh, A. R.; Jiang, G.; Zamani, P.; Song, Z.; Riese, A.; Harris, K. J.; Fu, X.; Chen, Z.; Sun, X.; Goward, G. R. Phosphorus and Nitrogen Centers in Doped Graphene and Carbon Nanotubes Analyzed through Solid-State NMR, *J. Phys. Chem. C* **2018**, *122* (12), 6593–6601. DOI: 10.1021/acs.jpcc.7b11671

[5] Zheng, Y.; Jiao, Y.; Li, L. H.; Xing, T.; Chen, Y.; Jaroniec, M.; Qiao, S. Z. Toward Design of Synergistically Active Carbon-Based Catalysts for Electrocatalytic Hydrogen Evolution, *ACS Nano* **2014**, *8* (5), 5290–5296. DOI: 10.1021/nn501434a

[6] Wu, H.; Chen, Z.; Wang, Y.; Cao, E.; Xiao, F.; Chen, S.; Du, S.; Wu, Y.; Ren, Z. Regulating the Allocation of N and P in Codoped Graphene: Via Supramolecular Control to Remarkably Boost Hydrogen Evolution, *Energy Environ. Sci.* **2019**, *12* (9), 2697–2705. DOI: 10.1039/c9ee00555b

[7] Zhang, C.; Mahmood, N.; Yin, H.; Liu, F.; Hou, Y. Synthesis of Phosphorus-Doped Graphene and Its Multifunctional Applications for Oxygen Reduction Reaction and Lithium Ion Batteries. *Adv. Mater.* **2013**, *25*, 4932–4937. DOI: 10.1002/adma.201301870

[8] Kapuria, A.; Mondal, T. K.; Shaw, B. K.; Su, Y. K.; Saha, S. K. Polysulfide Functionalized Reduced Graphene Oxide for Electrocatalytic Hydrogen Evolution Reaction and Supercapacitor Applications, *Int. J. Hydrogen Energy* **2023**, *48* (45), 17014–17025. DOI: 10.1016/j.ijhydene.2023.01.214

[9] Wang, J.; Yang, W.; Liu, J. CoP_2 Nanoparticles on Reduced Graphene Oxide Sheets as a Super-Efficient Bifunctional Electrocatalyst for Full Water Splitting, *J. Mater. Chem. A* **2016**, *4* (13), 4686–4690. DOI: 10.1039/c6ta00596a

[10] Liu, M.; Hof, F.; Moro, M.; Valenti, G.; Paolucci, F.; Pénicaud, A. Carbon Supported Noble Metal Nanoparticles as Efficient Catalysts for Electrochemical Water Splitting, *Nanoscale* **2020**, *12* (39), 20165–20170. DOI: 10.1039/d0nr05659f

[11] Creus, J.; De Tovar, J.; Romero, N.; García-Antón, J.; Philippot, K.; Bofill, R.; Sala, X. Ruthenium Nanoparticles for Catalytic Water Splitting, *ChemSusChem* **2019**, *12* (12), 2493–2514. DOI: 10.1002/cssc.201900393

[12] Romero, N.; Fenoll, D. A.; Gil, L.; Campos, S.; Creus, J.; Martí, G.; Heras-Domingo, J.; Collière, V.; Mesa, C. A.; Giménez, S.; Francàs, L.; Rodríguez-Santiago, L.; Solans-Monfort, X.; Sodupe,

M.; Bofill, R.; Philippot, K.; García-Antón, J.; Sala, X. Ru-Based Nanoparticles Supported on Carbon Nanotubes for Electrocatalytic Hydrogen Evolution: Structural and Electronic Effects, *Inorg. Chem. Front.*, 2023, **10**, 5885–5896. DOI: 10.1039/d3qi00698k

[13] Mallón, L.; Cerezo-Navarrete, C.; Romero, N.; Puche, M.; García-Antón, J.; Bofill, R.; Philippot, K.; Martínez-Prieto, L. M.; Sala, X. Ru Nanoparticles Supported on Alginate-Derived Graphene as Hybrid Electrodes for the Hydrogen Evolution Reaction. *New J. Chem.* **2022**, *46* (1), 49–56. DOI: 10.1039/d1nj05215b

[14] Shi, Y.; Dai, W.; Wang, M.; Xing, Y.; Xia, X.; Chen, W. Bioinspired Construction of Ruthenium-Decorated Nitrogen-Doped Graphene Aerogel as an Efficient Electrocatalyst for Hydrogen Evolution Reaction, *Chem. Res. Chin. Univ.* **2020**, *36* (4), 709–714. DOI: 10.1007/s40242-020-0167-2

[15] Zheng, B.; Ma, L.; Li, B.; Chen, D.; Li, X.; He, J.; Xie, J.; Robert, M.; Lau, T. C. pH Universal Ru@N-Doped Carbon Catalyst for Efficient and Fast Hydrogen Evolution. *Catal. Sci. Technol.* **2020**, *10* (13), 4405–4411. DOI: 10.1039/c9cy02552a

[16] Wang, J.; Wei, Z.; Mao, S.; Li, H.; Wang, Y. Highly Uniform Ru Nanoparticles over N-Doped Carbon: pH and Temperature-Universal Hydrogen Release from Water Reduction. *Energy Environ Sci* **2018**, *11* (4), 800–806. DOI: 10.1039/c7ee03345a

[17] Ye, R.; Liu, Y.; Peng, Z.; Wang, T.; Jalilov, A. S.; Yakobson, B. I.; Wei, S. H.; Tour, J. M. High Performance Electrocatalytic Reaction of Hydrogen and Oxygen on Ruthenium Nanoclusters. *ACS Appl. Mater. Interfaces* **2017**, *9* (4), 3785–3791. DOI: 10.1021/acsami.6b15725

[18] Cao, B.; Shi, H.; Sun, Q.; Yu, Y.; Chang, L.; Xu, S.; Zhou, C.; Zhang, H.; Zhao, J.; Zhu, Y.; Yang, P. Electron Deficiency Modulates Hydrogen Adsorption Strength of Ru Single-Atomic Catalyst for Efficient Hydrogen Evolution, *Renew. Energy* **2023**, *210*, 258–268. DOI: 10.1016/j.renene.2023.03.136

[19] Wang, W.; Tang, H.; Liu, H.; Li, S.; Liu, G.; Zhang, W.; Wang, Y.; Wang, Q.; Liu, Q. Modified Graphene Supported Ruthenium as an Efficient Electrocatalyst for Hydrogen Evolution Reaction in Alkaline Media, *Catal. Letters* **2023**, *154*, 1–10. DOI: 10.1007/s10562-023-04326-x

[20] Yang, Y.; Wu, D.; Yu, Y.; Li, J.; Rao, P.; Jia, C.; Liu, Z.; Chen, Q.; Huang, W.; Luo, J.; Deng, P.; Shen, Y.; Tian, X. Bridge the Activity and Durability of Ruthenium for Hydrogen Evolution Reaction with the Ru-O-C Link, *Chem. Eng. J.* **2022**, *433* (1), 134421. DOI: 10.1016/j.cej.2021.134421

[21] Nørskov, J. K.; Bligaard, T.; Logadottir, A.; Kitchin, J. R.; Chen, J. G.; Pandelov, S.; Stimming, U. Trends in the Exchange Current for Hydrogen Evolution. *J. Electrochem. Soc.* **2005**, *152* (3), J23–J26. DOI: 10.1149/1.1856988

[22] Greeley, J.; Nørskov, J. K.; Kibler, L. A.; El-Aziz, A. M.; Kolb, D. M. Hydrogen Evolution over Bimetallic Systems: Understanding the Trends, *ChemPhysChem* **2006**, *7* (5), 1032–1035. DOI: 10.1002/cphc.200500663

[23] Gutić, S. J.; Metarapi, D.; Jovanović, A. Z.; Gebremariam, G. K.; Dobrota, A. S.; Nedić Vasiljević, B.; Pašti, I. A. Redrawing HER Volcano with Interfacial Processes—The Role of Hydrogen Spillover in Boosting H_2 Evolution in Alkaline Media, *Catalysts* **2023**, *13* (1), 89. DOI: 10.3390/catal13010089

[24] Habibullah; Cen, W.; Wang, Y.; Yan, Y.; Chen, Y.; Wu, c. DFT study of Pd_4 and Pd_3P supported on modified graphene for hydrogen storage. *Int. J. Hydrog. Energy* **2024**, *50*, 659-669. DOI: 10.1016/j.ijhydene.2023.07.339

[25] Ješića, D.; Jurkovića, D. L.; Pohara, A.; Suhadolnikb, L.; Likozar, B. Engineering photocatalytic and photoelectrocatalytic CO_2 reduction reactions: Mechanisms, intrinsic kinetics, mass transfer resistances, reactors and multi-scale modelling simulations. *Chem. Eng. J.* **2021,** *407*, 126799. DOI:10.1016/j.cej.2020.126799

[26] Ganji, P.; Chowdari, R. K.; Likozar, B. Photocatalytic Reduction of Carbon Dioxide to Methanol: Carbonaceous Materials, Kinetics, Industrial Feasibility, and Future Directions. *Energy Fuels* **2023**, *37*, 7577−7602. DOI:10.1021/acs.energyfuels.3c00714

[27] Liu, T.; Wang, S.; Zhang, Q.; Chen, L.; Hu, W.; Li, C. M. Ultrasmall Ru_2P Nanoparticles on Graphene: A Highly Efficient Hydrogen Evolution Reaction Electrocatalyst in Both Acidic and Alkaline Media. *Chem. Commun.* **2018**, *54* (27), 3343–3346. DOI: 10.1039/c8cc01166d

[28] Liu, T.; Feng, B.; Wu, X.; Niu, Y.; Hu, W.; Li, C. M. Ru_2P Nanoparticle Decorated P/N-Doped Carbon Nanofibers on Carbon Cloth as a Robust Hierarchical Electrocatalyst with Platinum-Comparable Activity toward Hydrogen Evolution. *ACS Appl. Energy Mater.* **2018**, *1* (7), 3143–3150. DOI: 10.1021/acsaem.8b00334

[29] Axet, M. R.; Philippot, K. Organometallic Metal Nanoparticles for Catalysis. In *Nanoparticles in Catalysis: Advances in Synthesis and Applications*; Wiley-VCH Weinheim, 2021; pp 73–97.

[30] Martínez-Prieto, L. M.; Puche, M.; Cerezo-Navarrete, C.; Chaudret, B. Uniform Ru Nanoparticles on N-Doped Graphene for Selective Hydrogenation of Fatty Acids to Alcohols. *J. Catal.* **2019**, *377*, 429–437. DOI: 10.1016/j.jcat.2019.07.040

[31] Yang, T. T.; Patil, R. B.; McKone, J. R.; Saidi, W. A. Revisiting Trends in the Exchange Current for Hydrogen Evolution. *Catal. Sci. Technol.* **2021**, *11* (20), 6832–6838. DOI: 10.1039/d1cy01170g

[32] Saidi, W. A.; Yang, T. T. Reconciling the Volcano Trend with the Butler-Volmer Model for the Hydrogen Evolution Reaction. *J. Phys. Chem. Lett.* **2022**, *13* (23), 5310–5315. DOI: 10.1021/acs.jpclett.2c01411

[33] Cerezo-Navarrete, C.; Mathieu, Y.; Puche, M.; Morales, C.; Concepción, P.; Martínez-Prieto, L. M.; Corma, A. Controlling the Selectivity of Bimetallic Platinum-Ruthenium Nanoparticles Supported on N-Doped Graphene by Adjusting Their Metal Composition. *Catal. Sci. Technol.* **2021**, *11* (2), 494–505. DOI: 10.1039/d0cy02379e

[34] García-Zaragoza, A.; Cerezo-Navarrete, C.; Mollar-Cuni, A.; Oña-Burgos, P.; Mata, J. A.; Corma, A.; Martínez-Prieto, L. M. Tailoring Graphene-Supported Ru Nanoparticles by Functionalization with Pyrene-Tagged N-Heterocyclic Carbenes, *Catal. Sci. Technol.* **2022**, *12* (4), 1257–1270. DOI: 10.1039/d1cy02063c

[35] Latorre-Sánchez, M.; Primo, A.; García, H. P-Doped Graphene Obtained by Pyrolysis of Modified Alginate as a Photocatalyst for Hydrogen Generation from Water-Methanol Mixtures, *Angew. Chem. Int. Ed.* **2013**, *52* (45), 11813–11816. DOI: 10.1002/anie.201304505

[36] Yuan, B.; Xing, W.; Hu, Y.; Mu, X.; Wang, J.; Tai, Q.; Li, G.; Liu, L.; Liew, K. M.; Hu, Y. Boron/Phosphorus Doping for Retarding the Oxidation of Reduced Graphene Oxide, *Carbon* **2016**, *101*, 152–158. DOI: 10.1016/j.carbon.2016.01.080

[37] Creus, J.; Drouet, S.; Suriñach, S.; Lecante, P.; Collière, V.; Poteau, R.; Philippot, K.; García-Antón, J.; Sala, X. Ligand-Capped Ru Nanoparticles as Efficient Electrocatalyst for the Hydrogen Evolution Reaction. *ACS Catal.* **2018**, *8* (12), 11094–11102. DOI: 10.1021/acscatal.8b03053

[38] Costa, T. L. G.; Vieira, M. A.; Gonçalves, G. R.; Cipriano, D. F.; Lacerda, V.; Gonçalves, A. S.; Scopel, W. L.; de Siervo, A.; Freitas, J. C. C. Combined Computational and Experimental Study about the Incorporation of Phosphorus into the Structure of Graphene Oxide, *Phys. Chem. Chem. Phys.* **2023**, *25* (9), 6927–6943. DOI: 10.1039/d2cp03666e

[39] Navarro-Ruiz, J.; Rivera-Cárcamo, C.; Machado, B.; Serp, P.; Del Rosal, I.; Gerber, I. C. Computational Design of Pd Nanocluster and Pd Single-Atom Catalysts Supported on O-Functionalized Graphene. *ACS Applied Nano Materials* **2021**, *4* (11), 12235–12249. DOI: 10.1021/acsanm.1c02743

[40] Cusinato, L.; Del Rosal, I.; Poteau, R. Shape, electronic structure and steric effects of organometallic nanocatalysts: relevant tools to improve the synergy between theory and experiment. *Dalton Trans.* **2017**, *46*, 378–395. DOI: 10.1039/C6DT04207D

[41] Hammer, B.; Nørskov, J. K. Electronic Factors Determining the Reactivity of Metal Surfaces, *Surf. Sci.* **1995**, *343* (3), 211–220. DOI: 10.1016/0039-6028(96)80007-0

[42] Gerber, I. C.; Poteau, R. Critical assessment of charge transfer estimates in non-covalent graphene doping, *Theo. Chem. Acc.* **2018**, *137* (11), 156. DOI:10.1007/s00214-018-2365-2

[43] Martínez-Prieto, L. M.; Chaudret, B. Organometallic Ruthenium Nanoparticles: Synthesis, Surface Chemistry, and Insights into Ligand Coordination, *Acc. Chem. Res.* **2018**, *51* (2), 376–384. DOI: 10.1021/acs.accounts.7b00378

[44] Cusinato, L.; Martínez-Prieto, L. M.; Chaudret, B.; Del Rosal, I.; Poteau, R. Theoretical Characterization of the Surface Composition of Ruthenium Nanoparticles in Equilibrium with Syngas. *Nanoscale* **2016**, *8* (21), 10974–10992. DOI: 10.1039/c6nr01191h

[45] García-Antón, J.; Axet, M. R.; Jansat, S.; Philippot, K.; Chaudret, B.; Pery, T.; Buntkowsky, G.; Limbach, H. H. Reactions of Olefins with Ruthenium Hydride Nanoparticles: NMR Characterization, Hydride Titration, and Room-Temperature C-C Bond Activation, *Angew. Chemie Int. Ed.* **2008**, *47* (11), 2074–2078. DOI: 10.1002/anie.200704763